Theoretical and experimental investigation of Raman modes, ferroelectric and dielectric properties of relaxor Na0.5Bi0.5TiO3

Manish K. Niranjan, T. Karthik, Saket Asthana, Jaysree Pan, and Umesh V. Waghmare

---

Articles you may be interested in

Large strain response based on relaxor-antiferroelectric coherence in Bi0.5Na0.5TiO3–SrTiO3–(K0.5Na0.5)NbO3 solid solutions
J. Appl. Phys. **116**, 184104 (2014); 10.1063/1.4901549

Structural stability and depolarization of manganese-doped (Bi0.5Na0.5)1− x Ba x TiO3 relaxor ferroelectrics
J. Appl. Phys. **116**, 154101 (2014); 10.1063/1.4898322

Electric-field-induced and spontaneous relaxor-ferroelectric phase transitions in (Na1/2Bi1/2)1−xBaxTiO3
J. Appl. Phys. **112**, 124106 (2012); 10.1063/1.4770326

Dielectric and Raman scattering studies of phase transitions in the (100 − x) Na 0.5 Bi 0.5 TiO 3 – x SrTiO 3 system
J. Appl. Phys. **108**, 084102 (2010); 10.1063/1.3490781

Dielectric and ferroelectric properties of (Na 0.8 K 0.2) 0.5 Bi 0.5 TiO 3 thin films prepared by metalorganic solution deposition
Appl. Phys. Lett. **87**, 192901 (2005); 10.1063/1.2126129

Theoretical and experimental investigation of Raman modes, ferroelectric and dielectric properties of relaxor $Na_{0.5}Bi_{0.5}TiO_3$

Manish K. Niranjan,[1,a)] T. Karthik,[1,2] Saket Asthana,[1,b)] Jaysree Pan,[3] and Umesh V. Waghmare[3]

[1]*Advanced Functional Materials Laboratory and Department of Physics, Indian Institute of Technology, Hyderabad, India*
[2]*Department of Materials Science and Engineering, Indian Institute of Technology, Hyderabad, India*
[3]*Theoretical Sciences Unit, Jawaharlal Nehru Center for Advanced Scientific Research, Bangalore, India*

We use a combination of first-principles density functional theoretical analysis and experimental characterization to understand the lattice dynamics, dielectric and ferroelectric properties of lead-free relaxor ferroelectric $Na_{0.5}Bi_{0.5}TiO_3$ (NBT) system. Vibrational spectrum determined through our calculations agrees well with the observed Raman spectrum, and allows assignment of symmetry labels to modes. The calculated Born effective charges reveal (a) two distinct types of Ti ions at the *B*-site with anomalous dynamical charges differing by up $1.6e$, and (b) Na and Bi ions at the *A*-site exhibit disparate dynamical charges of about 1 and $5.5e$, respectively. Thus, there exist hetero-polar activity at both *A* and *B*-sites in NBT, and disorder associated with these hetero-polar ions is responsible for its relaxor behaviour. Large dielectric response of NBT arises primarily from phonons, and specifically the modes involving Bi-O ($109\,cm^{-1}$) and Ti-O (246, $276\,cm^{-1}$) vibrations, respectively. © *2013 AIP Publishing LLC*. [http://dx.doi.org/10.1063/1.4804940]

I. INTRODUCTION

Many devices such as sensors, actuators, accelerometers, etc., use lead based piezoelectric solid solutions near the morphotropic phase boundary (MPB). However, due to toxic nature of lead, there is a growing interest in the development of high performance lead-free piezoelectrics.[1–3] In recent years, $Na_{0.5}Bi_{0.5}TiO_3$ (NBT) and its solid solutions have emerged as promising alternative to lead-free piezoelectric compounds.[4–10] The NBT is a relaxor perovskite (ABO_3) with *A*-site being equally shared by two different cations, a property uncommon in most of the ABO_3 systems. The relaxor behavior of NBT is suggested to be due to cation disorder at the *A*-site (Na/Bi). As confirmed by recent neutron diffraction experiments, the NBT system undergoes several phase transitions in the temperature range of $5\,K$–$900\,K$.[11] At the room temperature, it stabilizes in rhombohedral structure with non-centrosymmetric *R3c* space group symmetry and shows unusual ferroelectric and dielectric properties.[11–13] The structure also exhibits anti-phase ($a^- a^- a^-$) TiO_6 octahedra tilting. Further, it exhibits a spontaneous polarization at the room temperature resulting from the cation displacements along the 3-fold [111] direction with remnant polarization value $P_r \cong 38\,\mu C/cm^2$ and a large coercive field $E_c \cong 70\,kV/cm$.[13] Even though the remnant polarization in NBT is strong, the large coercive field makes its piezoelectric properties undesirable. However, improved piezoelectric properties of NBT and its solid solutions by cation substitution at the *A* and *B*-sites have been reported.[14–20] In particular, NBT based solid solutions show significant improved piezoelectric behavior around the MPB region. Furthermore, their structural properties in terms of octahedral tilting and phase-coexistence at nanoscale level

were found to be quite interesting.[21–23] This has further fuelled the interest in NBT system as it remains to be understood the origin of various intrinsic properties and their structure-property correlations. In recent years, Raman and Infrared spectroscopic techniques have been used to study various structural aspects in NBT system and its solid solutions.[24–29] These techniques are advantageous as they provide precise information of local distortions and ionic configurations in the crystal structure.[30–32]

Reported theoretical studies on room temperature rhombohedral phase of NBT are relatively very few. In particular, no theoretical support exists to the experimentally measured Raman spectra, spontaneous polarization, dielectric properties, etc. In this paper, we address these issues within the *ab-initio* density functional theoretical framework, and identify spectroscopic signature of the rhombohedral structure through comparison with the experimental Raman spectrum. At the same time, the atomistic mechanisms are determined that may be relevant to the relaxor behavior of NBT.

This paper is organized as follows. The theoretical analysis is discussed in Sec. II with the computational details and the electronic structure of NBT in Secs. II A and II B, respectively. The results for spontaneous polarization, Born dynamical charges, zone-center phonon modes, and dielectric properties are discussed in Secs. II C–II E. The sample preparation and the X-ray diffraction analysis are described in Secs. III A and III B. The polarization, Raman, and dielectric measurements are discussed in Secs. III C–III E. Finally, we conclude in Sec. IV.

II. THEORETICAL DETAILS

A. Computational methodology

We use density functional theory (DFT) (Ref. 33) with the ultrasoft pseudopotentials (USPP) (Ref. 34) as

a)E-mail: manish@iith.ac.in. Tel.: (91)040-23016092. Fax: (91)040-23016032
b)E-mail: asthanas@iith.ac.in. Tel.: (91)040-23016067. Fax: (91)040-23016067

113, 194106-1

implemented in PWSCF (Ref. 35) package. The exchange-correlation energy is approximated within a local-density approximation (LDA). Kohn-Sham wave functions are expanded in plane wave basis with a kinetic energy cutoff of 35 Ry (and charge density with a cutoff of 280 Ry). We use $16 \times 16 \times 16$ Monkhorst-Pack k-point mesh for the Brillouin zone sampling. Self-consistency in calculations is achieved until the total energies are converged to 10^{-6} eV/cell, and the structures are relaxed until the largest force becomes less than 10^{-2} eV/Å. DFT-Linear response is used in determination of Born-effective charge tensors, dielectric permittivity tensors, and zone-centered phonon frequencies, with iterative Green's function approach of density-functional perturbation theory as implemented in PWSCF (Ref. 35) package.

B. Crystal and electronic structure of NBT

At room temperature, bulk NBT crystallizes in the non-centrosymmetric rhombohedral structure (space group $R3c$). Though Na and Bi atoms occupy A-site in disordered way, we use a unit cell consisting ten atoms (see Fig. 1) in our calculations, in which Na and Bi ions are ordered in a cell doubled along [111] axis of the perovskite structure. The z axis is taken along the 3-fold [111] axis. As given in Table I, the theoretical estimates of the lattice constant and angle (α) are in good agreement (within 1%–2%) with the experimental values (see Sec. III B). The calculated volume and the internal structural parameters (x,y,z) are within 4%–5% of experimental values.

In Fig. 2, we show the total and projected density of electronic states of NBT calculated at the optimized structural parameters. As evident from Figs. 2(a)–2(e), the valence band (VB) extends from -5 eV to 0 eV, and the states in the VB are primarily constituted of O-$2p$ states. There is a weak hybridization between O-$2p$ orbitals and (a) Bi-$6p$ at lower energy part of the VB, and (b) Ti-$3d$ orbitals in higher energy part of the VB. Such hybridization between cation and anion orbitals results in mixed ionic-covalent bonding in NBT, which is further evident from the anomalous Born effective charge tensor of Bi, Ti, and O ions (see Subsection II C). The covalent-ionic type bonding between Bi and O is expected as Bi^{3+} is isoelectronic to Pb^{2+}, and shows lone pair effect similar to that of Pb^{2+} in ferroelectric $PbTiO_3$.
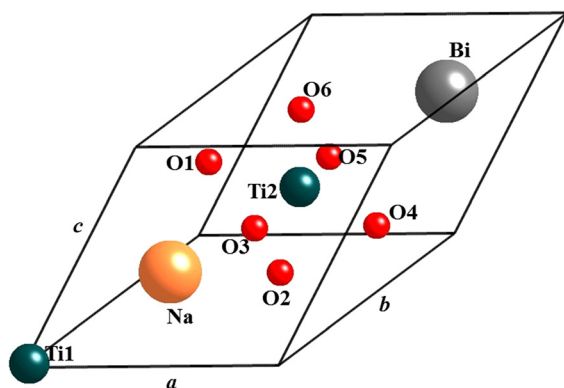
TABLE I. Theoretical and experimental lattice constant a_o (Å), angle α (in degrees), structural parameters (x,y,z), and volume Ω(Å^3) of $R3c$ NBT.

	Theory	Experiment (This work)	Ref. 11
a_o	5.421	5.4987	5.5051
α	59.499	59.7974	59.8027
Ω	111.4	117.02	117.7
Na/Bi			
x	0.2707	0.2611	0.2627
y	0.2707	0.2611	0.2627
z	0.2707	0.2611	0.2627
Ti			
x	0.0117	0.0063	0.0063
y	0.0117	0.0063	0.0063
z	0.0117	0.0063	0.0063
O			
x	0.1827	0.2070	0.2093
y	0.3140	0.2866	0.2933
z	0.7441	0.7496	0.7496

The cation-anion orbital hybridization suggests the ferroelectric order in NBT to be A- as well B-site driven. The states in the conduction band (CB) in the energy range 2.0–5.0 eV arise primarily from the Ti-$3d$ orbitals in addition to Bi-$6p$ states with weaker contribution.

C. Born effective charge tensors

Born effective charge tensor ($Z^*_{ij,\tau}$) of an atom τ is defined as the induced polarization along the direction i by a

FIG. 1. The rhombohedral ($R3c$) unit cell of NBT. The lattice constant, angle, and the structural parameters are given in Table I.
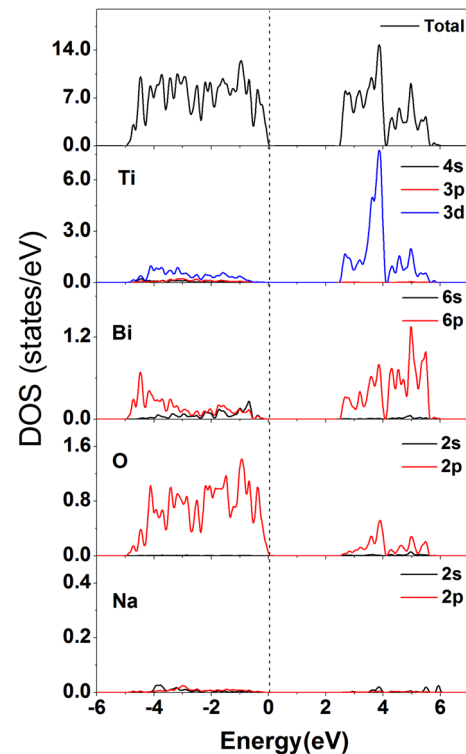

FIG. 2. (a) The total density of states of NBT. The partial density of states of NBT projected onto orbitals of (b) Ti atom, (c) Bi atom, (d) O atom, and (e) Na atom. Fermi energy is indicated by the dashed line.

TABLE II. Components of calculated Born effective charge tensors of Na, Bi, Ti, and O atoms in NBT. Last three columns show the eigenvalues of the symmetric part of the full tensor. (See Table I and Fig. 1 for position of atoms).

	Z^*_{xx}	Z^*_{xy}	Z^*_{xz}	Z^*_{yx}	Z^*_{yy}	Z^*_{yz}	Z^*_{zx}	Z^*_{zy}	Z^*_{zz}	Z^*_1	Z^*_2	Z^*_3
Na	1.11	−0.03	0.00	0.03	1.11	0.00	0.00	0.00	1.12	1.11	1.11	1.12
Bi	5.36	0.52	0.00	−0.52	5.36	0.00	0.00	0.00	4.02	5.36	5.36	4.02
Ti1	6.07	0.00	0.00	0.00	6.07	0.00	0.00	0.00	6.27	6.07	6.07	6.27
Ti2	7.15	−0.67	0.00	0.67	7.15	0.00	0.00	0.00	4.65	7.15	7.15	4.65
O1	−3.47	−0.74	−1.38	−0.68	−3.48	−1.16	−1.17	−1.23	−2.32	−5.23	−2.77	−1.27
O2	−4.09	0.32	1.70	0.38	−2.85	−0.61	1.65	−0.40	−2.32	−5.23	−1.27	−2.76
O3	−2.86	0.33	−0.32	0.39	−4.09	1.78	−0.48	1.63	−2.32	−5.24	−2.76	−1.27
O4	−4.02	−1.29	−0.81	−1.46	−2.17	−0.27	−0.83	−0.36	−3.04	−5.12	−1.43	−2.68
O5	−1.44	−0.03	0.17	−0.20	−4.75	0.83	0.10	0.89	−3.04	−1.43	−5.11	−2.68
O6	−3.83	1.57	0.63	1.40	−2.37	−0.57	0.72	−0.54	−3.04	−5.12	−1.44	−2.68

unit displacement in the direction j of the sublattice of atom τ. Anomalous value (deviation from the nominal charge) of Born charge is often an indicator of the role of the ion in contributing to ferroelectricity through off-centering, so called ferroactivity.[36] The calculated effective charge tensors of Na, Bi, Ti, and O atoms are presented in Table II. Due to higher local site symmetries of Na, Bi, and Ti atoms, their respective effective charge tensors are almost diagonal with at most two independent components. On the other hand, the Born effective charge tensors of O atoms are quite anisotropic with all the components being independent due to lower local site symmetry. As evident, the effective charges of Bi, Ti, and O atoms deviate significantly from their nominal ionic values, indicating the mixed ionic-covalent Bi-O and Ti-O bonding due to hybridization of O-$2p$ orbitals with Bi-$6p$ and Ti-$3d$ orbitals noted earlier. The charge tensor of Na atom is isotropic, and has only one independent component, and its value is quite close to its nominal ionic value of $+1$. This indicates that the Na-O bonding in NBT essentially remains ionic. The effective charge tensor of Bi atom has two independent components: one parallel ($Z^*_\parallel$) and two perpendicular ($Z^*_\perp$) to the rhombohedral [111] 3-fold axis. The calculated values of $Z^*_\perp$ ($+5.36$) and $Z^*_\parallel$($+4.02$) are higher than the ionic value of $+3$. Smaller value of the parallel component reflects that inversion symmetry along [111] axis already broken as it is the polar axis, and off-centering is still possible along directions perpendicular to [111] axis (reflected in soft modes, see Sec. II D). The Z^* tensor of Ti1 atom (see Fig. 1) located at (x,x,x) atom is diagonal and has two independent components: $Z^*_\parallel$ ($+6.26$) and $Z^*_\perp$ ($+6.06$). The Z^* of Ti2 located at $(^1/_2 + x_1, ^1/_2 + x_1, ^1/_2 + x_1)$ has a small antisymmetric off-diagonal component $Z^*_{xy}(-0.67)$ in addition to $Z^*_\parallel$ ($+4.64$) and $Z^*_\perp$ ($+7.15$). Here too, the charge tensor components are more anomalous along directions perpendicular to the polar axis. It is noteworthy that Z* of the two Ti ions is quite disparate, particularly along the polar axis. Thus, hetero-ferroactive (or heteropolar) disorder at both the A and B sites is expected to be relevant to the relaxor behavior of NBT, as noted earlier based on our findings on hybridization. The diagonal components of Z^* tensor of O atoms vary from -1.44 to -4.09.

Our estimate of the spontaneous polarization (P_s) of NBT obtained using the Berry phase method[37] is 26.3 μC/cm², in reasonable agreement with the experimental value of $P_s \cong$ 38 μC/cm² as shown in Fig. 4 (see later, Sec. III C).

D. Phonon frequencies at the Γ-point

The zone-center optical phonon modes of the $R3c$ phase of NBT in the absence of A-site disorder can be classified according to following irreducible representation:[38,39]

$$\Gamma = \underbrace{9A_1 \oplus 9E}_{Raman/IR}. \qquad (1)$$

The optical non-degenerate A_1 and doubly degenerate E modes are polarized along z-axis and in x-y plane, respectively. The A_1 and E optical modes are both Raman and IR active. However, when A-site disorder is taken into account, five of the IR/Raman modes with A_1 symmetry turn silent and the irreducible representation is modified as follows:[37]

$$\Gamma = \underbrace{4A_1 \oplus 9E}_{Raman/IR} \oplus \underbrace{5A_2}_{Silent}. \qquad (2)$$

Since we simulate a specific ordered configuration with a ten atom periodic cell in our calculations, we list calculated frequencies of the transverse (TO) and longitudinal (LO) optical modes in Table III according to the representation shown in Eq. (1). Overall, the agreement between the theory and experiment is reasonable. However, it should be noted that the experimental values listed in Table III are obtained at the room temperature rendering the direct comparison with the zero temperature theoretical values a bit tricky. The disagreement between the theoretical and experimental values can be attributed partially to the absence of A-site disorder in the theoretical model and the temperature difference.

The lowest frequency modes in the range of 109–134 cm⁻¹ are dominated by displacement of Bi ions. The modes in the frequency range of 155–187 cm⁻¹ and 246–401 cm⁻¹ are dominated by Na-O and TiO₆ vibrations, respectively, and higher frequency modes in the range 413–826 cm⁻¹ are primarily associated with the oxygen atoms vibrations. As evident from Table III, the LO-TO splitting is noticeable, as large as 180 cm⁻¹, but much weaker than that in ordered perovskites like PbTiO₃.

TABLE III. Fundamental frequencies (cm^{-1}) of NBT with their symmetry assignments. Experimental data were taken at the room temperature.

Mode	Theory	Experiment		
		This work	Ref. 24	Ref. 29
E(TO1)	109			
E(LO1)	130	120		
A_1(TO1)	134	141	131	142
A_1(LO1)	136			
E(TO2)	155			
E(LO2)	163			
A_1(TO2)	163	165		
A_1(LO2)	178			
E(TO3)	187			
E(LO3)	202			
A_1(TO3)	233	235		220
A_1(LO3)	234			
E(TO4)	246			
E(LO4)	300			
A_1(TO4)	276	274	279	281
A_1(LO4)	307	306		
E(TO5)	302			
E(LO5)	344			340
A_1(TO5)	317			
A_1(LO5)	398			
E(TO6)	349			
E(LO6)	412			
A_1(TO6)	401			
A_1(LO6)	410			
E(TO7)	413			
E(LO7)	444			
A_1(TO7)	428			
A_1(LO7)	469	490		491
E(TO8)	549	527	521	531
E(LO8)	591			
A_1(TO8)	575	573	576	585
A_1(LO8)	737	750	754	748
E(TO9)	594			
E(LO9)	774			
A_1(TO9)	825	820		803
A_1(LO9)	830	869	829	860

E. Dielectric permittivity tensors

The form of electronic (ε^∞) and the static (ε^0) dielectric permittivity tensors is determined by the symmetry of the crystal. For $R3c$ symmetry, there are two independent components ($\varepsilon_{||}$) and ($\varepsilon_\perp$) along and perpendicular to the 3-fold [111] axis, respectively. The average values of ε^∞ and ε^0 listed in Table IV are obtained by taking one-third of the trace of respective dielectric tensors. The calculated dielectric tensor component values are expected to be overestimated by about 10% due to underestimation of bandgaps in a DFT calculation. This error is generally attributed to the lack of polarization dependence in the exchange-correlation functional. The static dielectric tensor is calculated from the following classical dispersion formula:[40,41]

$$\varepsilon^0_{\alpha\beta} = \varepsilon^\infty_{\alpha\beta} + \sum_m \varepsilon_{m,\alpha\beta} = \varepsilon^\infty_{\alpha\beta} + \sum_m \frac{S_{m,\alpha\beta}}{m_0 \varepsilon_0 \Omega \omega^2_m}, \quad (3)$$

TABLE IV. Electronic and static dielectric tensors of NBT. The tensors are diagonal and have different components perpendicular ($\perp$) and parallel ($||$) to 3-fold [111] symmetry axis.

	ε^∞	$\varepsilon^\infty_\perp$	$\varepsilon^\infty_{||}$	ε^0	$\varepsilon^0_\perp$	$\varepsilon^0_{||}$
Theory	6.83	7.14	6.21	39.66	43.81	31.37
Exp.[a]	5.51					

[a]Reference 46.

where $\varepsilon^m_{\alpha\beta}$ is the contribution of the mth mode to the dielectric response, $S_{m,\alpha\beta}$ is the oscillator-strength of the mth mode, Ω is the primitive cell volume, ε_0 is the vacuum permittivity, and ω_m is the angular frequency of the mth mode. The oscillator strength ($S_{m,\alpha\beta}$) is related to the Born effective charge tensors ($Z^*_{\tau,\alpha\beta}$) and the eigenvectors ($\eta_m(\tau\beta)$) with the following:[42]

$$S_{m,\alpha\beta} = \left(\sum_{\tau\alpha'} Z^*_{\tau,\alpha\alpha'} \eta^*_m(\tau\alpha') \right) \left(\sum_{\tau'\beta'} Z^*_{\tau',\beta\beta'} \eta^*_m(\tau'\beta') \right). \quad (4)$$

Table V shows the parallel and perpendicular (to 3-fold [111] axis) components of mode effective charges and the mode contribution to the dielectric response. The mode effective charge ($Z^*_{m,\alpha}$) is defined as follows:[42]

$$Z^*_{m,\alpha} = \frac{\sum\limits_{\tau,\beta} Z^*_{\tau,\alpha\beta} \eta_m(\tau\beta)}{\sqrt{\sum\limits_{\tau,\beta} \eta^*_m(\tau\beta)\eta_m(\tau\beta)}}, \quad (5)$$

where $Z^*_{\tau,\alpha\beta}$ is the effective charge of ion τ, and $\eta_m(\tau\beta)$ is the eigenvector of the mth mode. The eigenvectors satisfy the following condition:

TABLE V. Components of mode effective charge vector (Z^*_m) and different mode contribution to static dielectric tensor perpendicular ($\perp$) and parallel ($||$) to 3-fold [111] symmetry axis.

Modes	$Z^*_{m,\perp}$	$Z^*_{m,||}$	$\varepsilon^0_\perp$	$\varepsilon^0_{||}$
E(TO1)	5.48	0.0	16.93	0.0
A_1(TO1)	0.0	1.67	0.0	1.68
E(TO2)	2.45	0.0	3.13	0.0
A_1(TO2)	0.0	2.79	0.0	5.71
E(TO3)	3.81	0.0	4.50	0.0
A_1(TO3)	0.0	0.78	0.0	0.3
E(TO4)	8.87	0.0	10.07	0.0
A_1(TO4)	0.0	6.67	0.0	11.7
E(TO5)	1.39	0.0	0.28	0.0
A_1(TO5)	0.0	3.18	0.0	2.58
E(TO6)	2.08	0.0	0.28	0.0
A_1(TO6)	0.0	0.80	0.0	0.05
E(TO7)	0.41	0.0	0.01	0.0
A_1(TO7)	0.0	1.95	0.0	0.51
E(TO8)	5.58	0.0	1.39	0.0
A_1(TO8)	0.0	4.93	0.0	1.99
E(TO9)	1.58	0.0	0.08	0.0
A_1(TO9)	0.0	0.72	0.0	0.02

$$\sum_{\tau\beta} M_\tau \eta_m^*(\tau\beta)\eta_n(\tau\beta) = \delta_{mn}, \qquad (6)$$

where M_τ is the mass of ion τ. The $A_1(TO4)$ and $E(TO4)$ modes with frequencies $276\,cm^{-1}$ and $246\,cm^{-1}$ exhibit highest mode effective charges resulting in high oscillator-strengths. These modes are associated with the TiO_6 vibrations. The highest contribution to the dielectric response in the plane perpendicular to the polar axis ([111]) comes from the lowest frequency E symmetry mode due to its high oscillator-strength and the frequency factor in Eq. (3). This mode primarily involves Bi-O displacements in addition to some degree of Ti-O displacements. In contrast, dielectric response along the direction parallel to the polar axis is dominated by the mode $A_1(TO4)$, mainly due to its large oscillator strength.

III. EXPERIMENTAL DETAILS

A. Sample preparation

Single phase NBT system is prepared by conventional solid state sintering technique using high purity precursors; Na_2CO_3, Bi_2O_3, TiO_2 (99.99% Sigma Aldrich Chemicals, USA). After loss of ignition, the precursors are weighed carefully according to proper stoichiometric ratios and subsequently milled and calcined at $800\,°C$ for $3\,h$. The calcined powders are further milled, sieved, and compacted into a circular disc. The disc is finally sintered at $1150\,°C$ for $3\,h$ in air atmosphere. Phase analysis of the sintered NBT sample is performed using powder x–ray diffractometer (PANlytical X'pert pro; Cukα radiation $\lambda = 1.5406\,\text{Å}$). Raman spectrum is obtained using a Laser Micro Raman spectrometer (Bruker, Senterra) in a back–scattering geometry with an excitation source of $532\,nm$. The power of laser spot on the polished sample surface is 10 mW, causing insignificant sample heating. The data are collected with frequency increment of $0.5\,cm^{-1}$ and with an integration time of $10\,s$. Polarization (P) vs. electric field (E) hysteresis measurements are obtained at $1\,Hz$ on the silver electroded NBT sample upto the maximum amplitude (i.e., the amplitude until dielectric breakdown occurs) using an TF-Analyzer 2000 (aixACCT systems, GmbH).

B. X-ray diffraction analysis:

Phase analysis of sintered NBT sample is performed using powder X-Ray diffraction. Before the XRD measurements, the finely grounded sample is annealed at $400\,°C$ to relieve the mechanical strains developed in the sample during grinding. Reitveld refinement (FULLPROF software package-version 2000) of the room temperature X-ray diffraction data is carried out for phase analysis using $R3c$ space group as a model. The refined parameters are summarized in Table I. Finally, our structural refinement shows a decent fit for $R3c$ model with an inset showing the magnified lower angle region indicating their goodness of fit (see Fig. 3). The refined NBT pattern also indicates the single phase characteristics with no other secondary phases being observed along with primary $R3c$ phase. The observed, calculated, and
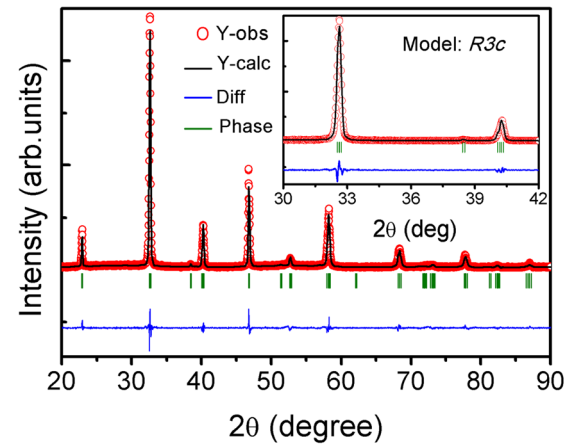

FIG. 3. Reitveld refined X-ray diffraction pattern of the sintered NBT sample with the inset showing the magnified lower angle region.

difference profiles from the final refinement are as follows: $R_p = 8.86$, $R_{wp} = 11.3$, and $\chi^2 = 1.94$.

C. Polarization measurements

P vs. E hysteresis measurement performed on NBT sample at $300\,K$ depicts a hard ferroelectric behavior with a large coercive field $E_C \cong 65\,kV/cm$ (i.e., $[(+E_C) + (-E_C)]/2$), along with a high remanent polarization value $P_r \cong 38\,\mu C/cm^2$ (i.e., $\pm P_r/2$) (see Fig. 4). Higher P_r value indicates that deficiency of Na/Bi is minimal and indicates the near ideal stoichiometry (i.e., $\cong Na_{0.5}Bi_{0.5}$).[13] However, a slight decrease in E_C values can be attributed to oxygen vacancies in the NBT system, due to higher sintering temperature.[43]

D. Raman measurements and analysis

Figure 5 shows the room temperature Raman scattering spectrum of the sintered NBT sample (polished surface). The observed Raman spectrum for NBT is consistent with previous reports.[24–29] It is observed that Raman modes of the NBT system are overlapped together and appear as four major bands labeled as A, B, C, and D (see Fig. 5). The deconvoluted phonon modes are tabulated in Table-III and are in good agreement with the theoretically calculated zone-
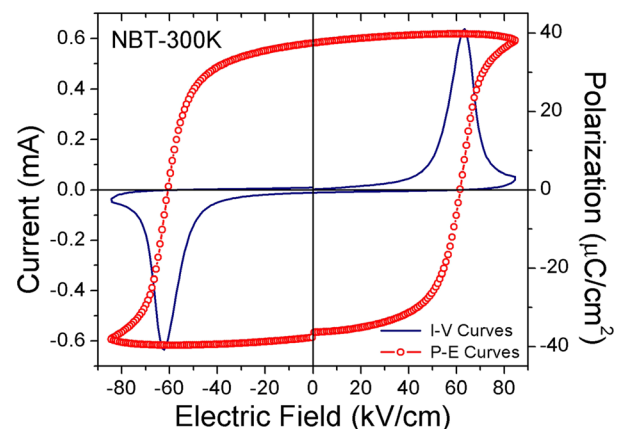

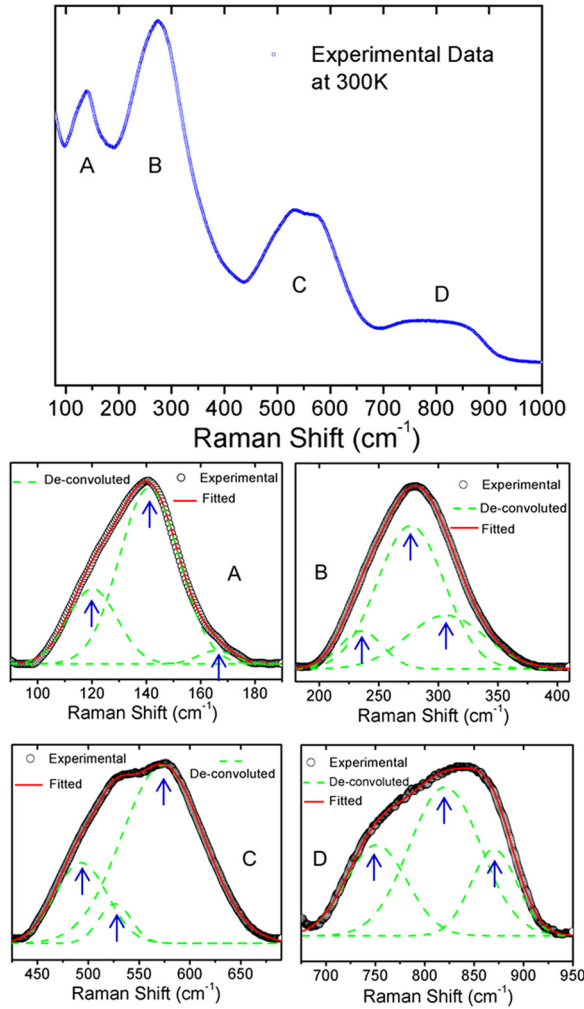FIG. 4. Room temperature P vs. E hysteresis loop and corresponding I-V curve of NBT sample.

FIG. 5. Raman spectrum of NBT sample measured at 300 K. The overlapped bands (A-D) have been de-convoluted into their individual components as indicated by arrows after base-line correction.

center phonon modes. It should be noted that symmetry mode assignment is not done for experimental values of phonon modes as an un-polarized laser beam is used. In Table III, the experimental mode values are compared with most closely matched theoretical values.

E. High temperature Impedance measurements and analysis

The temperature dependence of dielectric permittivity ($\varepsilon' = Cd/\varepsilon_o A$) and loss angle ($\tan\delta$) for NBT in the frequency range from 5 kHz to 1 MHz is shown in Figure 6(a). It is evident from the dielectric plot that ε' increases gradually with temperature until T_m (i.e., the transition temperature where the dielectric maximum occurs) and then decreases further with a diffused phase transition near T_m. The diffused phase transition is known to be one of the characteristic feature of relaxor ferroelctrics.[44,45] Though a strong frequency dependence in T_m is not observed (see Fig. 6(a)), the same is apparent in $\tan\delta$ near T_d (i.e., depolarization temperature) as shown in the inset of Fig. 6(a). The inverse dielectric permittivity ($1/\varepsilon'$) as a function of temperature is shown in Fig. 6(b). It is known that the ε' follows the
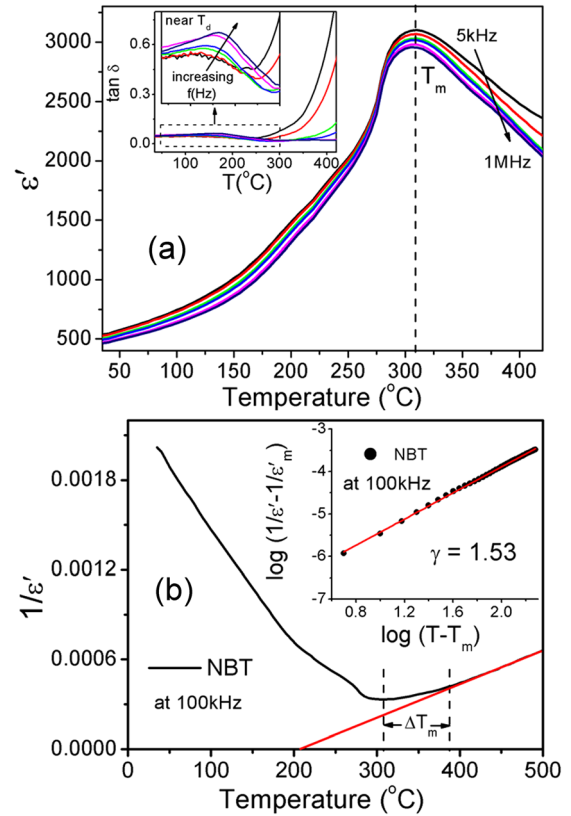

FIG. 6. (a) ε' vs. T (°C) plot depicting diffused phase transition near T_m (i.e., $\cong$ 310 °C for 100 kHz data) along with $\tan\delta$ vs. T (°C) in the inset of Fig. 6(a). (b) Curie-Weiss ($1/\varepsilon'$ vs T(°C)) and diffusivity plots (inset of Fig. 6(b)) indicating the relaxor behavior of NBT.

Curie-Weiss law, $\varepsilon' = C/(T - T_{CW})$, in paraelectric regime in conventional ferroelectric materials. Here, the C and T_{CW} are Curie-weiss constant and Curie-Weiss temperature, respectively.[44,45] As seen in Fig. 6(b), the ε' vs. T deviates from the Curie-Weiss behavior in NBT due to disorder. The order of diffusivity or disorderness in NBT can be analyzed using modified Curie-Weiss law: $1/\varepsilon' - 1/\varepsilon'_m = (T - T_m)^\gamma/C$ where γ is the diffusivity parameter and T_m is the temperature at which ε' is maximum (ε_m). The diffusivity parameter (γ) is calculated from the slope of $\log(1/\varepsilon' - 1/\varepsilon'_m)$ vs $\log(T - T_m)$ plot as shown in the inset of Fig. 6(b). The value of γ approaches 1 in case of a conventional ferroelectric, whereas it is 2 for an ideal relaxor ferroelectric.[45,46] For NBT, the γ is found to be 1.53 (at 100 kHz) indicating that the phase transition is diffusive. The relaxor feature in NBT may be attributed to cation disorder and their heteropolar nature as discussed in Sec. II C.

IV. CONCLUSIONS

The structural, electronic, lattice dynamical, and dielectric properties of the relaxor ferroelectric NBT are studied experimentally as well as from first-principles calculations. A reasonably good agreement is obtained between the experimentally observed structure, Raman modes, and spontaneous polarization and those obtained from the theoretical calculations. The Born effective charges of ions are found to be anisotropic, in particular, those of oxygen. The Born

effective charges of Bi and Ti ions are significantly larger than their nominal charges, particularly in direction perpendicular to the 3-fold [111] symmetry axis. Further, they show hetero-polarity of ions at both *A* and *B* sites, disorder between which is the atomistic feature relevant to relaxor properties. In addition, the mode-effective Born charges and contribution of different modes to the dielectric response are determined. The lowest frequency mode (109 cm^{-1}) involving Bi-O vibrations dominates the dielectric response along the polar direction, while modes at 246 and 276 cm^{-1} involving TiO$_6$ vibrations are found to contribute significantly to the dielectric response in the plane perpendicular to the polar direction. We hope our study will further stimulate theoretical and experimental studies of NBT with disorder at *A* site and associated lattice dynamical properties.

ACKNOWLEDGMENTS

[1]Y. Saito, H. Takao, T. Tani, T. Nonoyama, K. Takatori, T. Homma, T. Nagaya, and M. Nakamura, Nature (London) **432**, 84 (2004).

[2]E. Cross, Nature (London) **432**, 24 (2004).

[3]J. Rodel, W. Jo, K. T. P. Seifert, E.-M. Anton, T. Granzow, and D. Damjanovic, J. Am. Ceram. Soc. **92**, 1153–1177 (2009).

[4]Y.-M. Chiang, G. W. Farrey, and A. N. Soukhojak, Appl. Phys. Lett. **73**, 3683 (1998).

[5]Y. Guo, M. Gu, H. Luo, Y. Liu, and R. L. Withers, Phys. Rev. B **83**, 054118 (2011).

[6]Y. Hiruma, H. Nagata, and T. Takenaka, J. Appl. Phys. **105**, 084112 (2009).

[7]W. Jo, T. Granzow, E. Aulbach, J. Rodel, and D. Damjanovic, J. Appl. Phys. **105**, 094102 (2009).

[8]J. E. Daniels, W. Jo, J. Rodel, and J. L. Jones, Appl. Phys. Lett. **95**, 032904 (2009).

[9]J. Kreisel, P. Bouvier, B. Dkhil, P. A. Thomas, A. M. Glazer, T. R. Welberry, B. Chaabane, and M. Mezouar, Phys. Rev. B **68**, 014113 (2003).

[10]V. A. Shuvaeva, D. Zekria, A. M. Glazer et al., Phys. Rev. B **71**, 174114 (2005).

[11]G. O. Jones and P. A. Thomas, Acta Crystallogr., Sect. B: Struct. Sci. **58**, 168–178 (2002).

[12]J. Suchanicz, Mater. Sci. Eng., B **55**, 114–118 (1998).

[13]M. Spreitzer, M. Valant, and D. Suvorov, J. Mater. Chem. **17**, 185–192 (2007).

[14]T. Takenaka, K. Maruyama, and K. Sakata, Jpn. J. Appl. Phys. **30**, 2236–2239 (1991).

[15]V. A. Isupov, Ferroelectrics **315**, 123–147 (2005).

[16]M. Davies, E. Aksel, and J. L. Jones, J. Am. Ceram. Soc. **94**(5), 1314–1316 (2011).

[17]Y. Hiruma, Y. Imai, Y. Watanabe, H. Nagata, and T. Takenaka, Appl. Phys. Lett. **92**, 262904 (2008).

[18]M. D. Drahus, P. Jakes, E. Erdem, S. Schaab, J. Chen, M. Ozerov, S. Zvyagin, and R.-A. Eichel, Phys. Rev. B **84**, 064113 (2011).

[19]N. Lei, M. Zhu, P. Yang, L. Wang, L. Wang, Y. Hou, and H. Yan, J. Appl. Phys. **109**, 054102 (2011).

[20]E. Aksel, J. S. Forrester, B. Kowalski, M. Deluca, D. Damjanovic, and J. L. Jones, Phys. Rev. B **85**, 024121 (2012).

[21]W. Jo, J. E. Daniels, J. L. Jones, X. Tan, P. A. Thomas, D. Damjanovic, and J. Rodel, J. Appl. Phys. **109**, 014110 (2011).

[22]J. Yao, N. Monsegue, M. Murayama, W. Leng, W. T. Reynolds, Q. Zhang, H. Luo, J. Li, W. Ge, and D. Viehland, Appl. Phys. Lett. **100**, 012901 (2012).

[23]C. W. Tai and Y. Lereah, Appl. Phys. Lett. **95**, 062901 (2009).

[24]I. G. Siny, E. Husson, J. M. Beny, S. G. Lushnikov et al., Ferroelectrics **248**, 57 (2000).

[25]J. Kreisel, A. M. Glazer, G. Jones, P. A. Thomas, L. Abello, and G. Lucazeau, J. Phys.: Condens. Matter **12**, 3267 (2000).

[26]J. Kreisel, A. M. Glazer, P. Bouvier, and G. Lucazeau, Phys. Rev. B **63**, 174106 (2001).

[27]B. W. van Eerd, D. Damjanovic, N. Klein, N. Setter, and J. Trodahl, Phys. Rev. B **82**, 104112 (2010).

[28]D. Rout, K.-S. Moon, S. Joong, L. Kang, and I. W. Kim, J. Appl. Phys. **108**, 084102 (2010).

[29]J. Suchanicz, I. J. Sumara, and T. V. Kruzina, J. Electroceram. **27**, 45–50 (2011).

[30]H. Taniguchi, H. O. Soon, T. Shimizu, H. Moriwake, Y. J. Shan, and M. Itoh, Phys. Rev. B **84**, 174106 (2011).

[31]A. Dias, A. Khalam, L. Mailadil, T. Sebastian, C. William, A. Paschoal, and R. L. Moreira, Chem. Mater. **18**, 214–220 (2006).

[32]W. Zhang, Z. Wang, and X. M. Chen, J. Appl. Phys. **110**, 064113 (2011).

[33]W. Kohn and L. J. Sham, Phys. Rev. **140**, A1133 (1965).

[34]D. Vanderbilt, Phys. Rev. B **41**, 7892 (1990).

[35]P. Giannozzi et al., J. Phys.: Condens. Matter **21**, 395502 (2009).

[36]U. V. Waghmare, N. A. Spaldin, H. C. Kandpal, and R. Seshadri, Phys. Rev. B **67**, 125111 (2003).

[37]R. D. King-Smith and D. Vanderbilt, Phys. Rev. B **47**, 1651 (1993).

[38]J. Petzelt, S. Kamba, J. Fábry, D. Noujni, V. Porokhonskyy, A. Pashkin, I. Franke, K. Roleder, J. Suchanicz, R. Klein, and G. E. Kugel, J. Phys.: Condens. Matter **16**, 2719–2731 (2004).

[39]D. L. Rousseau, R. P. Bauman, and S. P. S. Porto, J. Raman Spectrosc. **10**, 253 (1981).

[40]M. Born and K. Huang, *Dynamical Theory of Crystal Lattices* (Oxford University Press, Oxford, 1954).

[41]X. Gonze and C. Lee, Phys. Rev. B **55**, 10355 (1997).

[42]G.-M. Rignanese, X. Gonze, and A. Pasquarello, Phys. Rev. B **63**, 104305 (2001).

[43]K. Ishii, D. Isshiki, Y. Ohki, H. Nishikawa, and M. Takiyama, Jpn. J. Appl. Phys., Part 1 **34**, 205 (1995).

[44]D. Viehland, S. J. Jang, L. Eric Cross, and M. Wuttig, Phys. Rev. B **46**, 8003 (1992).

[45]K. Datta, P. A. Thomas, and K. Roleder, Phys. Rev. B **82**, 224105 (2010).

[46]M. Bousquet, J. R. Duclere, E. Orhan, A. Boulle, C. Bachelet, and C. Champeaux, J. Appl. Phys. **107**, 104107 (2010).